

Probing the Hot Gaseous Halo of the Low-mass Disk Galaxy NGC 7793 with eROSITA and Chandra

LIN HE,^{1,2} ZHIYUAN LI,^{1,2,3} MEICUN HOU,³ MIN DU,⁴ TAOTAO FANG,⁴ AND WEI CUI⁵

¹*School of Astronomy and Space Science, Nanjing University, Nanjing 210023, China*

²*Key Laboratory of Modern Astronomy and Astrophysics, Nanjing University, Nanjing 210023, China*

³*Institute of Science and Technology for Deep Space Exploration, Suzhou Campus, Nanjing University, Suzhou 215163, China*

⁴*Department of Astronomy, Xiamen University, Xiamen, Fujian 361005, China*

⁵*Department of Astronomy, Tsinghua University, Beijing 100084, China*

ABSTRACT

Galaxy formation models predict that local galaxies are surrounded by hot X-ray-emitting halos, which are technically difficult to detect due to their extended and low surface brightness nature. Previous X-ray studies have mostly focused on disk galaxies more massive than the Milky Way, with essentially no consensus on the halo X-ray properties at the lower mass end. We utilize the early-released eROSITA and archival *Chandra* observations to analyze the diffuse X-ray emission of NGC 7793, a nearby spiral galaxy with an estimated stellar mass of only $3.2 \times 10^9 M_{\odot}$. We find evidence for extraplanar hot gas emission from both the radial and vertical soft X-ray intensity profiles, which spreads up to a galactocentric distance of ~ 6 kpc, nearly 30% more extended than its stellar disk. Analysis of the eROSITA spectra indicates that the hot gas can be characterized by a temperature of $0.18_{-0.03}^{+0.02}$ keV, with 0.5–2 keV unabsorbed luminosity of 1.3×10^{38} erg s⁻¹. We compare our results with the IllustrisTNG simulations and find overall consistence on the disk scale, whereas excessive emission at large radii is predicted by TNG50. This work provides the latest detection of hot corona around a low-mass galaxy, putting new constrains on state-of-the-art cosmological simulations. We also verify the detectability of hot circumgalactic medium around even low-mass spirals with future high-resolution X-ray spectrometer such as the Hot Universe Baryon Surveyor.

1. INTRODUCTION

It is a long-standing prediction of galaxy formation models that a rarefied, volume-filling hot gas corona exists around most present-day (disk) galaxies (White & Rees 1978), giving rise to the soft X-ray emission with a characteristic temperature of 10^{6-7} K. Two prevailing scenarios have been proposed for its origin: In an external way, the intergalactic medium (IGM) gas confines to the galaxy and gets gravitationally heated, leaving a hot halo surrounding the disk when the gas cooling time exceeds the free-fall timescale (White & Rees 1978; White & Frenk 1991). In an internal channel, galactic feedback processes, such as stellar winds and supernovae (SNe), thermalize and metal-enrich the ambient medium, further entrain them to the halo via the driving of outflows/winds (Mathews & Baker 1971; Chevalier & Clegg

1985). In the meantime, feedback from an active galactic nucleus (AGN) can also impact the hot gaseous halo by driving vertical outflows which can transport the energy, momentum and metals (Choi et al. 2020). As one would expect, this X-ray-emitting hot corona (also known as hot circumgalactic medium [CGM]) is a very complicated reservoir mixing the accreted IGM, the star-formation-enriched outflowing gas and the recycling flows, and it potentially occupies a significant fraction of the cosmic missing baryons.

In spite of their fundamental importance, the detection and characterization of galactic hot gas halos is challenging, owing to a low gas density. The thermal Sunyaev-Zeldovich (SZ) effect and soft X-ray emission are two routinely used tools to explore this hot phase CGM. The former, aiming to measure the distortion of the Cosmic Microwave Background (CMB) power spectrum arising from the inverse Compton scattering of CMB photons by free electrons, is generally sensitive to massive clusters/groups and the measurements of CGM have used ensembles of galaxies splitted into different

helin@smail.nju.edu.cn

lizy@nju.edu.cn

mass bins to achieve a reliable detection (Bregman et al. 2018, 2022; Planck Collaboration et al. 2013; Greco et al. 2015). On the other hand, while the hot gas halo emits in soft X-rays, the signals can be very weak and often overwhelmed by galactic stellar sources. Efforts have been made to detect the diffuse X-ray emission in nearby spiral galaxies (Li et al. 2007; Li & Wang 2007; Dai et al. 2012; Anderson & Bregman 2011; Bogdán et al. 2013a,b; Walker et al. 2015; Li et al. 2016, 2017), relying on various X-ray missions (ROSAT, *Chandra* and XMM-Newton), and it has led to the consensus that hot gas halos are ubiquitous in massive spirals, with their X-ray luminosity scaled with the star formation rate (SFR) (Li & Wang 2013a; Li et al. 2014). Moreover, dedicated studies for a few giant spirals (e.g. NGC 1961, Anderson et al. 2016; NGC 6753, Bogdán et al. 2017) find a negative gradient of the temperature and a rather flat, sub-solar metallicity profile for the galactic hot gas, hinting at the predominant role of IGM accretion as its origin.

However, there is less consensus on the physical properties (e.g. mass, temperature, metallicity) and the spatial distribution of hot gas in and around less massive L_* galaxies (especially for $M_* < M_{\text{MW}}$). In theory, the virialized halo gas will have a temperature of $T_v = \frac{2}{3} \frac{GM_v}{r_v} \frac{\mu m_H}{k_B}$ (Benson 2010), where M_v and r_v are the galaxy's virial mass and radius, G and k_B are the gravitational and Boltzmann constant, μ is the mean molecular mass, and m_H is the atomic mass unit. Thus galaxies at the low-mass end are predicted to have halos with lower temperature, less emissivity, and are more difficult to detect. Alternatively, stellar feedback, in the form of galactic outflows/winds, is thought to play a key role in the gas replenishment of the hot corona surrounding less massive galaxies. Diffuse X-ray emission emerging from the hot coronal gas has been detected in both starburst dwarf galaxies (Ott et al. 2005) and archetypical starburst disk galaxies (e.g., M82, Lehnert et al. 1999; NGC 253 Strickland et al. 2002), with its spatial distribution elongated along the direction of the maximum pressure gradient. Additional examples can be found in a systematic study of galactic coronae around nearby highly inclined disk galaxies conducted by Li & Wang (2013b), which covers a broad range of SFR and stellar masses. It would be valuable to investigate if the feedback-related hot coronae are ubiquitous from actively star-forming dwarf galaxies to normally star-forming L_* galaxies, and if they share a common origin.

A major limitation is that current sample of galactic hot gaseous halo has modest size and is biased to massive disk galaxies in the local universe. Specifically, there

is still an unsatisfactory lack of individual detections in low-mass galaxies (e.g., non-detections in Bothun et al. 1994; Bomans 2001; Mulchaey & Jeltema 2010; Hou et al. 2021, 2024). Stacked measurements of this diffuse and faint component have been obtained thanks to the wide-field X-ray survey such as the ROSAT All-Sky Survey (RASS), the eROSITA Final Equatorial Depth Survey (eFEDS) and its all-sky survey (eRASS, Bogdán et al. 2015; Anderson et al. 2013; Chadayammuri et al. 2022; Zhang et al. 2024a,b; Zhang et al. 2024). By accumulating signals from a large number of galaxies, the diffuse X-ray emission arising from the hot CGM can be captured and is found to spread out to hundreds of kiloparsec for galaxies at various mass bins. However, drawbacks of this method are obvious: (1) the resolution of stacked signals are generally poor (~ 10 kpc for ROSAT stackings of Milky Way size galaxies at a median redshift of $z \sim 0.08$), and hence can not bring out the internal structure of CGM; (2) the removal of contribution from groups and clusters along the line of sight poses theoretical and technical challenges, hence the contamination is inevitable. For this reason, individual measurements are still valuable to help us better understand the galaxy formation theory and put tighter constraints on state-of-the-art cosmological simulations.

Launched in 2019, eROSITA (extended ROentgen Survey with an Imaging Telescope Array) was designed to perform sensitive wide-field sky surveys, with sensitivity enhanced more than thirtyfold compared with ROSAT (Predehl et al. 2021). This telescope contains seven identical Wolter-1 mirror modules, achieving an effective area (2400 cm² at 1 keV) much larger than that of *Chandra* and a moderate angular resolution (15'' on-axis) comparable to XMM-Newton. The large field of view of eROSITA (~ 1 degree in diameter) will enable us to depict the large-scale vicinity of nearby galaxies and track the elusive hot X-ray corona out to large radii, which is costly for *Chandra* and XMM-Newton. It holds promise to detect the diffuse X-ray emission from a large number of galaxies and to provide a statistically representative sample for galactic X-ray studies.

NGC 7793, with a stellar mass of $3.2 \times 10^9 M_\odot$ (Bothwell et al. 2009) and an SFR of $0.52 M_\odot \text{ yr}^{-1}$ (Calzetti et al. 2015), is one of the brightest galaxies in the Sculptor Group, the nearest constellation of galaxies outside our Local Group. It is classified as an Sd galaxy with a very tiny bulge and chaotic spiral arms. This bulgeless characteristic, along with its moderate stellar mass, makes it controversial to fuel a MBH and contain large volumes of hot gas. Besides, this galaxy is famous for harboring a powerful microquasar (Pakull et al. 2010), which ejects collimated jets strong

enough to inflate a fast-expanding bubble spanning ~ 300 parsecs in diameter. In virtue of its proximity (at a distance of 3.91 Mpc, Karachentsev et al. 2003) and the peculiarity, it has a wealth of data including HST, Spitzer, GALEX, VLA, MUSE, XMM-Newton and *Chandra*, along with a planned JWST observation. Deep observations have shown that its H α and H I emission easily extend to or beyond the optical radius R_{25} , both manifesting a truly declining rotational curve (Carignan & Puche 1990; Dicaire et al. 2008). The diffuse ionized gas accounts for $\sim 40\%$ of the its H α emission, and can be detected reaching the edge of the H I disk, making the H II disk of this galaxy one of the largest ever observed among the non-active late-type systems. However, its galactic X-ray emission remains relatively underexplored, especially for the measurement of halo gas. Pannuti et al. (2011) conducted a *Chandra* ACIS observation to study the supernova remnants (SNRs) in NGC 7793. In addition, they found that the galaxy’s diffuse X-ray emission can be characterized by a temperature of 0.19–0.25 keV. A ROSAT PSPC observation (Read & Pietsch 1999) has detected the rather uniform unresolved emission in and around NGC 7793, extending out to ~ 4 kpc with a higher temperature of $kT \sim 1$ keV. The discrepancy of the gas temperature may primarily lie in the much broader point spread function (PSF) wings of ROSAT PSPC, which led to the contamination of more spillover harder X-ray photons from the point sources. Moreover, due to the relatively poor sensitivity of ROSAT, the diffuse emission is also heavily contaminated by unresolved stellar sources, which is expected to be mitigated in the eROSITA era.

This paper is organized as follows: in Section 2, we describe the observation and data preparation. The results and analysis, including the radial (vertical) perspective of the diffuse X-ray emission distribution and spectral analysis, are presented in Section 3. We compare our results with TNG50 simulations in Section 4 and discuss the implications in Section 5. Our main conclusions are summarized in Section 6. Throughout this work, we assume a flat Λ CDM cosmology with $\Omega_m = 0.3$, $\Omega_\Lambda = 0.7$, and $H_0 = 70 \text{ km s}^{-1} \text{ Mpc}^{-1}$. All uncertainties are quoted at 1σ confidence level unless stated otherwise.

2. OBSERVATION AND DATA PREPARATION

2.1. eROSITA

NGC 7793 was observed by eROSITA as part of the Calibration and Performance Verification (Cal-PV) program. A pointed observation (ObsID: 300011) was conducted on NGC 7793 utilizing all 7 eROSITA telescope

modules (TMs), with an effective exposure time of ~ 51.2 ks and a covered field of diameter ~ 1 deg. The eROSITA data reduction was performed using the extended Science Analysis Software System (eSASS, Brunner et al. 2022) and the eROSITA Calibration Database (CALDB). As the TM5 and TM7 are reported to be heavily contaminated by light leak at low energies, we adopt an energy filter of $PI > 400$ to avoid this effect following previous eROSITA studies¹. We focus our analysis on three energy bands: the soft (0.4–1.0 keV), hard (1.0–2.3 keV) and full band (0.4–2.3 keV). We first generated the counts and vignetting-corrected exposure maps in each band using the *evtool* and *expmap* task, merging data derived from all 7 TMs. The argument `gti="FLAREGTI"` was additionally adopted to filter out the potential soft proton flares. Next we created the corresponding instrumental background maps from the Filter Wheel Closed (FWC) data. To be consistent with the released calibrated event file, we specified `flag=0xC000F000` to remove strongly vignettted corners of the square CCDs and `pattern=15` to select single, double, triple, and quadruple patterns. The instrumental background for all the 7 TMs were merged, preparing for the following analysis.

Liu et al. (2022) carried out source detection for 11 extra-galactic CalPV fields and presented a serendipitous catalog containing 9522 X-ray sources, among which 647 individuals are in the N7793 field. In view of its relatively large point spread function (PSF) wings, we masked the detected sources by circles of the 90% enclosed energy radius (EER), adjusting to 1.5 times 90% EER for some very bright point sources. All the counts, exposure and instrumental background maps were uniformly filtered off the detected X-ray sources for the following analysis. It is noteworthy that this procedure still cannot completely eliminate a few extended sources, including SNRs in the disk of NGC 7793 and background galaxy groups or clusters, which may contribute to some excesses in the final intensity profiles (see details in Section 3.1 and Section 3.2).

2.2. Chandra

NGC 7793 has five publicly available *Chandra* observations by October 2022. All five observations had their

¹ We have compared the results when excluding and including the light-leak affected TM5 & TM7 and found no significant differences. We thus retain all the seven TMs but adopt a relatively higher lower energy bound, in order to better probe the putative faint diffuse emission. Similar treatments to the light leak contamination can also be found in Zhang et al. (2024a) and Veronica et al. (2024)

Table 1. X-ray Observations of NGC 7793

Observing Date	ObsID	Exposure	R.A.	Dec.
eROSITA				
2019-11-18	300011-1	53.8	23:57:51.00	-32:37:27.0
<i>Chandra</i>				
2003-09-06	3954	42.5	23:57:49.75	-32:35:29.5
2011-08-13	14231	58.5	23:57:59.90	-32:33:20.9
2011-12-25	13439	57.4	23:57:59.90	-32:33:20.9
2011-12-30	14378	24.7	23:57:59.90	-32:33:20.9
2020-06-04	23266	29.7	23:57:51.00	-32:37:26.6

NOTE—The exposure time for eROSITA is the effective unvignetted exposure time averaged over the 7 TMs. The exposure times for *Chandra* have values after filtering the soft proton flares. All exposures are in units of ks.

aim-point on the S3 CCD of the Advanced CCD Imaging Spectrometer (ACIS), which was placed within 3' from the galactic center. We included data from the S2, S3, I2 and I3 CCDs to maximize the useful field-of-view (FoV; covering a galactocentric radius up to $\sim 15'$) and the signal-to-noise ratio (S/N). The data reduction is performed using CIAO v4.13² and CALDB v4.9.5, following the standard procedures as described in Hou et al. (2021). We produce the counts and exposure maps on the natal pixel scale of $0.492''$ in the 0.5–1, 1–2 and 0.5–2 keV band, from which the time intervals contaminated by soft proton flares were filtered out for each observation, resulting in a total effective exposure of ~ 210 ks. We also generated the corresponding instrumental background maps from the stowed background files, after normalizing with the 10–12 keV count rate. The counts, instrumental background and exposure maps were then reprojected to a common tangential point, i.e., the optical center of the galaxy to produce the combined images.

Using the CIAO tool *wavdetect*, we detected 142 point sources across the whole field in the 0.5–2 keV band, supplying the 50% encircled energy fraction (EEF) PSF map and adopting a detection threshold of 10^{-6} and scales of 1, 2, 4, 8 and 16 pixels. A notable population of discrete point sources emerge from the galactic disk including the microquasar and its two hotspots in nebula S26, a well-studied ultraluminous X-ray source (ULX) P13, and a faint point source positionally coincident with the galactic nucleus (see white dashed circles in Figure 1c). For the purpose of studying the diffuse X-ray emission, pixels falling in two times the 90% EER

of each detected point source were removed, consistently for the counts, background and exposure maps.

3. ANALYSIS AND RESULTS

An eROSITA false-color image of the NGC 7793 field is shown in Figure 1a, revealing a large number of point sources as well as extended X-ray features in and around the galaxy, out to a projected distance of $30'$ thanks to eROSITA's large FoV. In particular, two bright clumps are found to the southwest of NGC 7793, which have been identified as background galaxy clusters, as label in Figure 1a. A possible third cluster (or galaxy group) is seen near the northwest corner of the field, although we find no available classification or redshift for this feature. The *Chandra* view of NGC 7793, which has a smaller field than eROSITA, is shown in Figure 1c, offering more details on the galactic disk thanks to its superb angular resolution and the deep on-axis exposure. We also utilize publicly available data from other wavebands to constrain the distribution of the stellar content, warm ionized gas and atomic hydrogen. The composite image shown in Figure 1b includes H I data from VLA (red), H α line emission (green) and B-band data (blue) from the CTIO 1.5-m telescope. We outline the optical disk of NGC 7793 with a cyan ellipse. The semi-major axis ($a = 4.65'$) and semi-minor axis ($b = 3.15'$) are adopted from the NASA/IPAC Extragalactic Database (NED³), which is determined from the B-band isophote of 25.0 mag arcsec⁻² (de Vaucouleurs et al. 1991). The diffuse X-ray emission detected by eROSITA is shown by yellow contours.

3.1. Radial Intensity Profile

The eROSITA 0.4–2.3 keV flux image is generated by subtracting the instrumental background from the counts image and dividing the remainder by the exposure map, as displayed in Figure 2. For a better visualization, all the removed point sources are refilled by sampling counts from their surrounding background and the image has been smoothed with a Gaussian kernel of 5 pixels in radius. The galactic disk and the brighter part of the diffuse X-ray emission are outlined by contours as in Figure 1b. We mark ten brightest point sources in this field with green crosses. Diffuse features are apparent at some of these positions, which might be partly due to the incomplete removal of these bright sources. The two or three background clusters also clearly stand out in this image, but they show no clear boundaries, making it difficult to mask out their potential contamination to the putative hot gas halo of NGC 7793. Hence in the

² <http://cxc.harvard.edu/ciao/>

³ <http://ned.ipac.caltech.edu/>

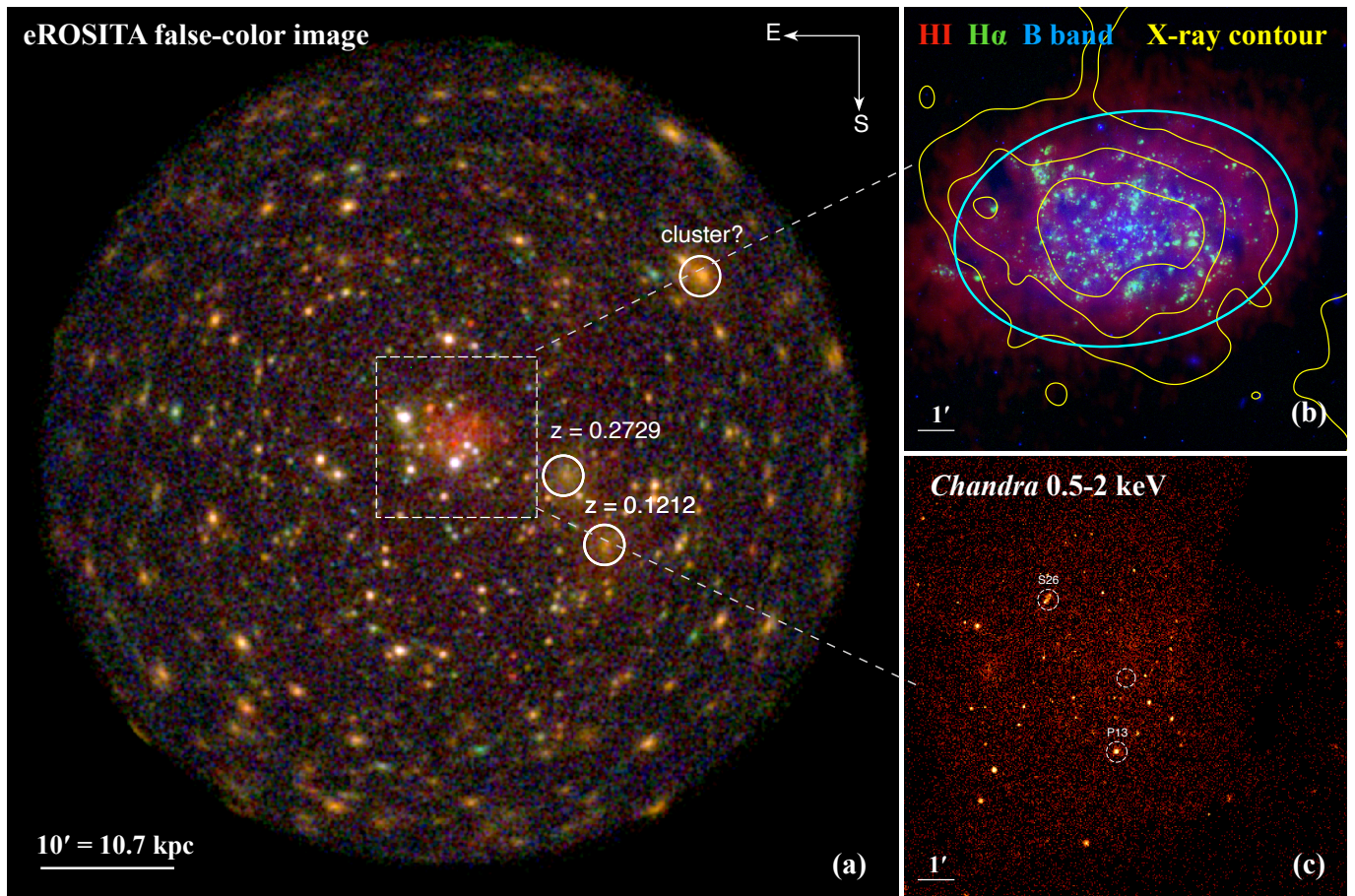


Figure 1. *Left:* the eROSITA false-color image of the NGC 7793 field. The red channel corresponds to 0.4–1 keV, green to 1–2.3 keV, and blue to 2.3–5 keV. The white dashed box encloses the central $12' \times 12'$ region. Two background clusters in southwest are circled and deliberately omitted in the analysis. *Upper right:* The composite image of H I (red), H α (green) and B-band (blue), with the 0.4–2.3 keV diffuse X-ray emission in yellow contours (derived from eROSITA flux map with the location of removed point sources refilled by sampling their surrounding background), at intensity levels of $3.5, 7.0, 10.5 \times 10^{-4}$ cts s^{-1} arcmin $^{-2}$. The D_{25} ellipse in cyan has a diameter of $9.3' \times 6.3'$. *Lower right:* the combined Chandra counts map in the energy band of 0.5–2.0 keV, zoomed-in as the composite image. The ULX P13 and the nebula S26 are marked with white dashed circles. Also marked by a dash circle is the X-ray nucleus, which, despite being faint, is revealed for the first time after stacking the five observations.

following quantitative analysis we discard the western half of the field unless otherwise stated.

To quantify the extent of the apparently diffuse X-ray emission, we extract the radial intensity profiles for eROSITA in the 0.4–2.3 keV band, as well as for *Chandra* in the 0.5–2 keV band, as shown in Figure 3. The profiles are adaptively binned to achieve a S/N greater than 5. We note that the variation of sensitivity across the FoV has a non-negligible effect on the large-scale X-ray emission. The reduced sensitivity at larger off-axis angles makes it harder to resolve the faint point sources (mostly background AGNs) and hence bring heavier contamination to the diffuse emission, which manifests as an uplift of the radial intensity profile at large radii. To correct for this residual cosmic X-ray background (i.e., to achieve a statistically

uniform source removal across the FoV), we construct a second background map from the empirical X-ray $\log N$ - $\log S$ relation derived by Georgakakis et al. (2008) (see details in Appendix A), taking into account the source detection sensitivity across the FoV. The thus created eROSITA radial intensity profile in Figure 3 has subtracted this residual cosmic background, an effect on the level of 10%, which is supported by the apparent flatness of the profile at large radii. The stacked *Chandra* image shows highly non-uniform exposure and hence an even larger variation in the point-source sensitivity across the field. Therefore we have also corrected this effect for the *Chandra* intensity profile.

Comparing the two panels of Figure 3, the eROSITA and *Chandra* intensity profiles look qualitatively quite similar to each other, showing an inward rising compo-

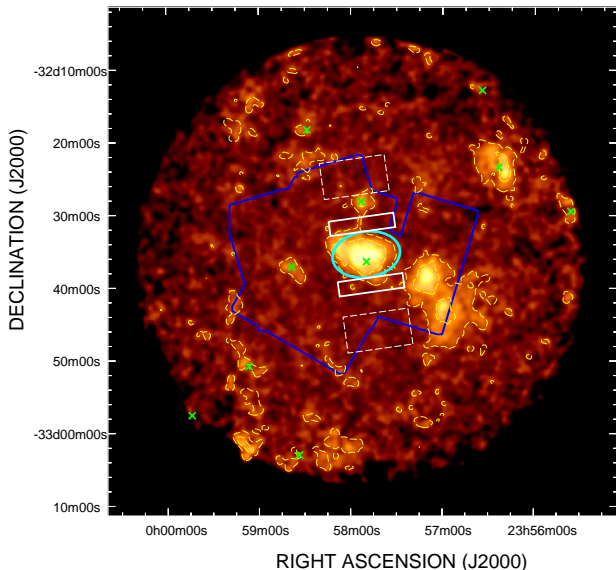


Figure 2. eROSITA instrumental background subtracted, exposure corrected image in the energy band of 0.4–2.3 keV. The image has been smoothed with a Gaussian kernel size of 5 pixels, and the point sources have been removed and refilled by sampling their surrounding background. The galactic disk is indicated by the D_{25} ellipse in cyan, while the diffuse X-ray emission is outlined by yellow contours at intensity levels of $3.5, 7.0, 10.5 \times 10^{-4} \text{ cts s}^{-1} \text{ arcmin}^{-2}$. The two $9' \times 2'$ solid rectangles show the spectral extracted regions of the putative north and south halo, while the two dashed rectangles show the adopted background regions. We mark the positions of ten brightest point sources in this field with green crosses. The *Chandra* footprint is also shown in blue.

ment corresponding to the galactic emission and a flat component at large radii ($\gtrsim 10'$) representing the local sky background. On top of this, both profiles exhibit several local dips (or excesses), which can be understood as due to absorption by the spiral arms or the excessive emission from bright point sources. However, a noteworthy dip appears at $6'–8'$ (indicated by the arrows in Figure 3), which is unlikely to be affected by the H I disk, as the column density has decreased down to 10^{20} cm^{-2} at radius of $\sim 5'$ and hence the local absorption cannot explain this dip feature. Moreover, we have examined the eROSITA profiles in two subbands: 0.4–1 keV and 1–2.3 keV, finding that the dip is even more prominent in the higher energy band, which further argues against being due to absorption. The possibility of instrumental artifact has also been ruled out, as both the eROSITA and *Chandra* data show the same feature. We discuss the potential origins of this peculiar dip in Section 5.

To have a phenomenological understanding of the diffuse X-ray emission, we fit the radial intensity profiles with a β -model ($I_X = I_0[1 + (r/r_c)^2]^{0.5-3\beta}$, describing the sum of hot gas and unresolved stellar sources),

with an additional constant characterizing the sky background. Both the eROSITA and *Chandra* profiles show no highly enhanced central emission and the fitted r_c tends to converge to $\sim 5'$, suggesting a large core radius of $\sim 5 \text{ kpc}$. The best-fit results are $\beta = 1.60_{-0.47}^{+0.51}$ and $I_0 = 16.29_{-0.42}^{+0.42} \times 10^{-4} \text{ cts s}^{-1} \text{ arcmin}^{-2}$ for eROSITA, and $\beta = 1.18_{-1.67}^{+1.69}$, $I_0 = 14.55_{-1.61}^{+1.58} \times 10^{-4} \text{ cts s}^{-1} \text{ arcmin}^{-2}$ for *Chandra*. The level of sky background is indicated by horizontal lines in Figure 3. It is shown that the diffuse X-ray emission can be traced out to $5'–6'$ (equaling to 5–6 kpc in physical scale), which is up to 30% more extended than the starlight, in spite of the existence of the peculiar dip.

3.2. Vertical Intensity Profile

To study the X-ray emission genuinely from the so-called hot corona, contributions from the galactic disc, which often overwhelm the former and involve various unresolved stellar sources, have to be taken into account appropriately. For edge-on galaxy, it is straightforward to differentiate the corona from the disc according to the scale height of galactic plane (typically $\sim 1 \text{ kpc}$). With an inclination of 50° (Tully 1988), NGC 7793 is close to the most moderately inclined spirals in Li & Wang (2013b), which studied a sample of 53 nearby highly-inclined disc galaxies with $i \gtrsim 60^\circ$ using *Chandra* observations. We thus extract the vertical intensity profiles of eROSITA in the energy band 0.4–2.3 keV, as well as the *Chandra* 0.5–2 keV, H α and H I surface brightness profile, to define the vertical range of corona gas.

We obtain such profiles along both the major-axis and minor-axis, with a running length of $6'$ to ensure a nearly full coverage in the *Chandra* stacked image. The negative direction corresponds to the east (south) and positive to the west (north), for the major- (minor-) axis. As is illustrated in Figure 4, all the profiles have been renormalized according to the eROSITA intensities within the central $\pm 1'$ for ease of comparison. It is worth noting that the X-ray data has been subtracted off the sky background to isolate the pure galactic contribution. The *Chandra* profile, although less informative due to the steeply declining exposure at large offset, is consistent with the eROSITA profile. The horizontal lines are identical to those in the radial profiles and indicate the sky background level. Notably, the diffuse soft X-ray emission shows some asymmetry in both the central and off-disk regions along different directions, which may arise from residual contamination by point sources and/or from localized feedback processes. At least a few abrupt excesses are attributed to the the incompletely removed sources: Along the major-axis, the bump at $\sim -4'$ corresponds to a bright source first discovered by

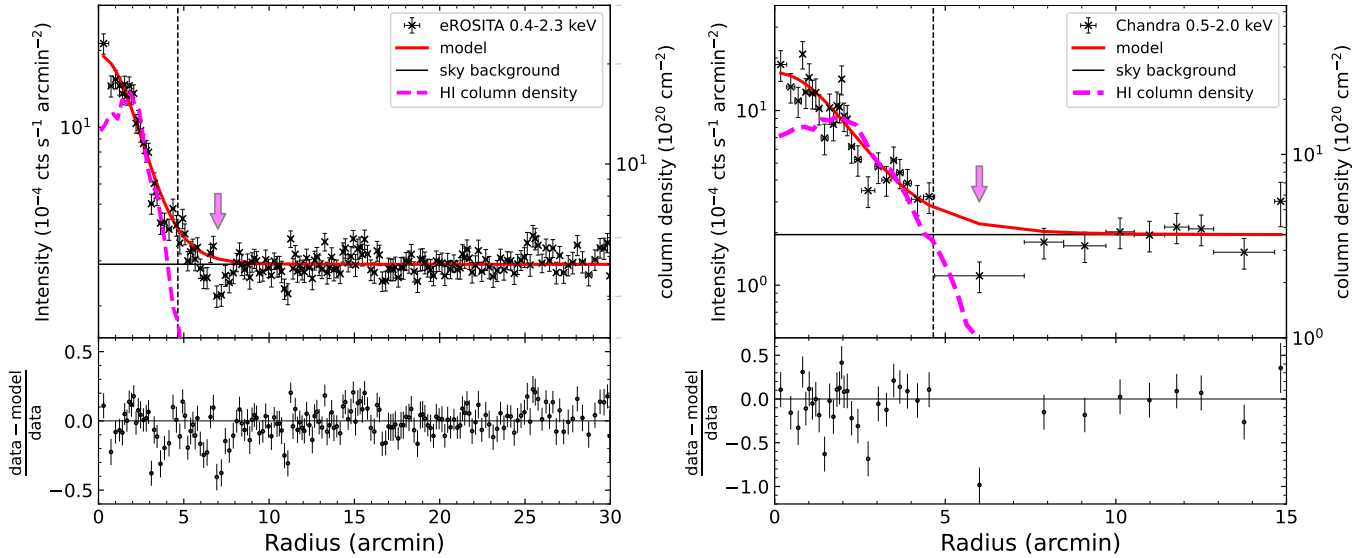


Figure 3. *Left:* Instrumental background-subtracted, exposure-corrected radial intensity profile of *eROSITA* in the energy band of 0.4–2.3 keV, adaptively binned to achieve a S/N greater than 10. The magenta curve shows the H I column density, which is derived from a high resolution VLA H I map scaled with a low resolution KAT-7 column density map (Sorgho et al. 2018). The grey horizontal line indicates the level of sky background. The red curve represents the β +sky model, which is used to roughly characterize the diffuse X-ray distribution. *Right:* Same as *Left*, but for the radial intensity profile of *Chandra* in the energy band of 0.5–2.0 keV, adaptively binned to achieve a S/N greater than 5.

Read & Pietsch (1999) (P9 in that work), whose identity is still uncertain and the X-ray spectrum is very steep ($\Gamma \sim 2.4$) and absorbed. Another bump at 8′–9′ on the positive side most likely arises from the northern edge of the background cluster ($z=0.2729$). Nevertheless, the X-rays averagely exceed the scaled H α emission from the inner 3′ along both the major- and minor-axis, suggestive of the presence of extraplanar diffuse X-ray emission. The H I emission of NGC 7793 otherwise stretches far, with extension comparable to the X-ray along both directions. This extended H I disk of NGC 7793, as well as its truly declining rotation curve, has been reported by Carignan & Puche (1990), hinting at a centrally concentrated dark matter halo. When incorporating the vertical profiles and the X-ray contours (see Figure 2), we note that the extraplanar X-ray emission is not manifested as a bipolar or biconic feature. This suggests that the underlying physical origin of the hot gas may differ from the classical vertical outflows observed in some archetypical superwind galaxies (e.g., NGC 253, M82). However, more dedicated investigations, such as azimuthal analysis, are currently hindered by the relatively low photon counts and the presence of background clusters in the vicinity.

3.3. Spectral Analysis

Since we are mainly interested in the genuine hot corona of NGC 7793, contributions from the galactic plane, which dominate the diffuse X-ray emission, need to be marginalized in the spectral analysis. The spec-

tral extraction was performed using the *srctool* task. We use two symmetrical rectangle regions with length of 9′ along major-axis and inner-to-outer side of $\pm 3.15′$ – $5.15′$ along minor-axis as the source regions (i.e. the north corona and south corona), deliberately avoiding the stellar disk. The corresponding background spectra are extracted from two box regions parallel to the source region, each with a size of 9′ \times 5′. The white dashed boxes in Figure 2 outline the extraction regions, within which all discrete point sources have been carefully removed for the spectral analysis.

The spectra are adaptively regrouped to achieve a signal-to-noise ratio greater than 3. We adopt an optically thin plasma model (APEC in *Xspec*) to characterize the diffuse hot gas, with an additional power-law component needed to describe the emission from the residual point sources (i.e., the XRBs and residual CXB). Both components are subject to the Galactic foreground absorption toward NGC 7793 ($N_{\text{H}} = 3 \times 10^{20} \text{ cm}^{-2}$). The abundance is poorly constrained and thus fixed at half solar. We find that this model yields similar power-law photon-index and plasma temperature for the spectrum of the north and south corona, with the difference in fluxes being less than a factor of two. Hence the spectra have been co-added to achieve a higher S/N and better constrain the parameters. The combined spectrum is displayed in Figure 5, with the best-fit model characterized by a temperature of $0.18_{-0.03}^{+0.02} \text{ keV}$ for the hot plasma (orange)

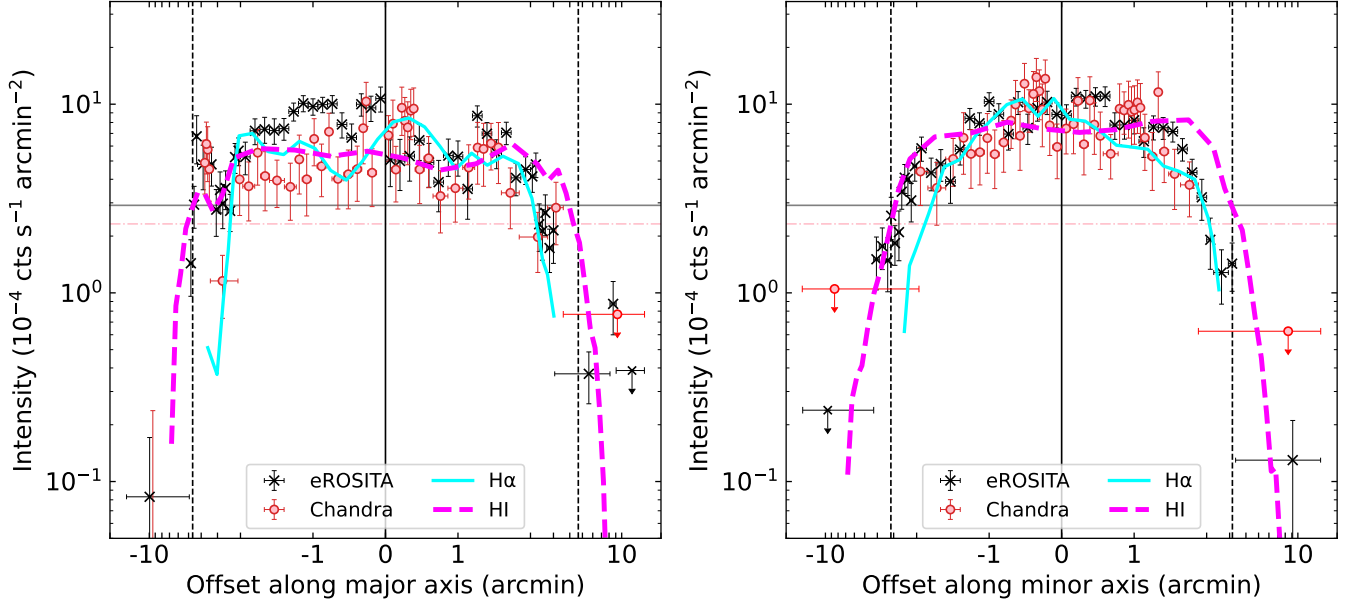


Figure 4. *Left:* Sky and instrumental background-subtracted, exposure-corrected vertical intensity profile of *eROSITA* along the major-axis in the energy band of 0.4–2.3 keV (black), adaptively binned to achieve an S/N greater than 3. Vertical profiles of *Chandra* (red), H α (cyan) and H I (magenta) fluxes are overlaid after normalizing to the *eROSITA* intensity. The outermost bins, which lack sufficient statistics to satisfy S/N > 3, are represented by upper limits. The horizontal black (pink) line indicates the sky background of *eROSITA* (*Chandra*). The semi-major axis at $\pm 4.65'$ are marked by black dashed lines. We use a ‘symlog’ scale for the x-axis to prevent excessive crowding of data points in the central region, thereby significantly improves the readability. *Right:* Same as *Left*, but along the minor-axis. The semi-minor axis at $\pm 3.15'$ are marked by black dashed lines.

and a photon-index of $1.67^{+0.34}_{-0.38}$ for the power-law component (blue). Although the fit is not so satisfactory ($\chi^2/d.o.f = 34.22/23$), the data quality is insufficient to introduce more complicated models, thus we adopt it since the results appear to be physical and reasonable.

Surprisingly, the derived halo gas temperature is similar to that of the warm-hot phase gas in the Milky Way’s halo (Yoshino et al. 2009; Gupta et al. 2021; Das et al. 2021; Kaaret et al. 2020; Locatelli et al. 2024; Bhattacharyya et al. 2023). However, we note that the local background (including the emission from the Galactic halo, the Local Hot Bubble and unresolved CXBs) has been subtracted from the source spectrum, so contamination from the Milky Way’s hot gas halo is minimal and the detected 0.18 keV hot plasma is most likely to originate from NGC 7793 itself. This similarity in temperature may be taken as a hint of the ubiquitous hot halo around L_* galaxies. We estimate the enclosed hot gaseous mass from the APEC normalization, which gives a value of $\sim 1 \times 10^7 M_\odot$. By comparison, the neutral gas mass of NGC 7793 is $M_{\text{HI}} \sim 6.8 \times 10^8 M_\odot$ (Walter et al. 2008, a slightly higher value was given by LVHIS, Koribalski et al. 2018). The unabsorbed 0.5–2 keV luminosity of the hot gas is $1.27 \pm 0.33 \times 10^{38} \text{ erg s}^{-1}$. The unresolved point sources contribute a 0.5–2 keV flux of $1.28 \pm 0.23 \times 10^{-13} \text{ erg s}^{-1} \text{ cm}^{-2}$, translating to luminosity of $2.33 \pm 0.42 \times 10^{38} \text{ erg s}^{-1}$ at the distance of

NGC 7793. We highlight that the extraction region occupies a minor fraction in terms of the generically predicted X-ray halo, which is thought to be quasi-spherical and has a large volume. The actual distribution of the hot gas (e.g. its geometry and the volume filling factor), is still unknowable due to the high sky background and the limiting sensitivity.

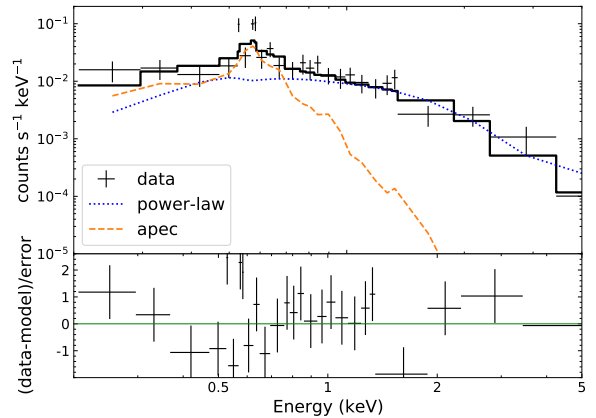


Figure 5. *eROSITA* spectrum for the extraplanar unresolved X-ray emission of NGC 7793 and the best-fit model. The spectral data has been regrouped to achieve a signal-to-noise ratio of 3. The fitted model is $tbabs \times (\text{powerlaw} + \text{apec})$, and the power-law and apec components are shown in blue and orange, respectively.

4. COMPARISON WITH THE TNG50 SIMULATION

The detected extraplanar X-ray emission of NGC 7793, originating from the putative hot gaseous corona, is not common in normal low-mass (both early- and late-type) galaxies (Bothun et al. 1994; Bomans 2001; Hou et al. 2021, 2024). Here we compare our X-ray measurements with the influential TNG50 simulation to shed light on the hot gaseous corona around NGC 7793-like galaxies.

4.1. TNG50 Simulation and Sample Selection

We utilize the data from Illustris-TNG (Nelson et al. 2019a,b; Pillepich et al. 2019), a suite of state-of-the-art cosmological simulations carried out using the AREPO moving-mesh code. Specifically, we employ TNG50, which is designed to simulate a large, representative cosmological volume at a numerical resolution approaching the modern zoomed-in simulations of individual galaxies. It evolves 2160³ gas cells in a (51.7 cMpc)³ box with best spatial resolution of 74 parsecs and a baryonic mass resolution of $8.5 \times 10^4 M_{\odot}$, which is sufficient to provide a detailed look at the gas structure around galaxies.

We use the last snapshot ($z=0$) of TNG50 to search for simulated galaxies resembling NGC 7793. Our selection criteria are as follows: (1) $10^{9.2} < M_{*}/M_{\odot} < 10^{9.6}$ and $10^{11} < M_{\text{halo}}/M_{\odot} < 10^{12}$, to construct a representative sample of galaxies in a suited mass range; (2) $M_{\text{gas}}/(M_{\text{gas}} + M_{*}) > 0.1$, where M_{gas} is the mass of cold gas with $T < 10^{4.5}$ K, to exclude gas-poor galaxies; (3) primary flag = 1, to exclude satellite galaxies whose halo gas may be strongly impacted by the central galaxy. After these steps, we identify 460 candidates. To further refine our selection to galaxies with clear disk structures, we use the catalog derived from Du et al. (2019, 2020), which decomposed the simulated galaxies into well-defined structures (i.e., disk, bulge, and stellar halo). We additionally require our simulated counterparts having ‘‘Spheroids’’ < 0.5 (total mass fraction for kinematically identified bulge and halo structures) to ensure they are disk-dominated. This leaves us a final sample of 297 galaxies, with SFR ranged from 0.03 to 1.41 $M_{\odot} \text{ yr}^{-1}$. To clarify, the involved galaxy properties are defined as follows: the stellar mass (M_{*}) refers to the total mass of star particles which are bound to the subhalo, and SFR refers to the sum of individual SFRs of all gas cells in a certain galaxy.

4.2. Hot Gas Emission in TNG50 Galaxies

To investigate the X-ray-emitting hot gas in the simulated galaxies, we consider all gas cells with a temperature higher than $10^{5.5}$ K, which is roughly the virial temperature for galaxies with such mass range. We

generate X-ray spectral templates using the PyAtomDB code (Foster & Heuer 2020), which gives the spectrum of hot plasma in collisional ionization equilibrium at a given temperature. Based on the general understanding that metallicity gradients are present in galaxies, the predicted spectra have taken into account both temperature and metallicity of each gas cell. The total X-ray luminosity in a volume is obtained by integrating the emission of all enclosed hot gas cells in the energy range of 0.5–2 keV.

We produce the radial and vertical X-ray luminosity profiles for each simulated galaxy using the particle-level data. To match with the observations, each galaxy was rotated to have an inclination angle of 50° and projected to the X-Y plane. Given the majority of our sample galaxies are relatively poorly resolved due to their small mass, we adopt a conservative bin size for the radial and vertical profiles, i.e., 0.5 kpc for each bin. A horizontal length of 6 kpc for the vertical bins is adopted to be consistent with the observations. The predicted profiles from TNG50 simulations are shown in the left column of Figure 6. The overlaid observational data points are obtained by converting the measured photon fluxes to 0.5–2 keV luminosities, assuming an apc model with temperature and abundance of the best-fit values in Section 3.3. We have subtracted the same sky (local) background as in Figure 3 and Figure 4 from the observational data and thus the profiles represent the real emission from hot gas in and around NGC 7793.

As is illustrated, the observations are consistent with simulations to some degree, both for the radial and vertical perspective. However, the innermost bins (within 1 kpc) of eROSITA and *Chandra* data exhibit a rather flat trend, quite distinct from the simulated results that hot gas emission is notably enhanced in the central region compared to the outer disk. The prediction of brighter-than-observed compact cores in TNG and EAGLE simulations is also reported by Comparat et al. (2022). From galactocentric radius of 3 kpc, the observational data points start to lie systematically below the median value of simulations, indicating excessive hot gaseous content around low-mass disk galaxies predicted by TNG50 simulations. This discrepancy, however, can also be understood as NGC 7793 being an exception, given the fact that a representative sample of observed hot gas halo around low-mass disk galaxies is still lacking, which would otherwise yield strong constraints on the galaxy formation models reflected by these state-of-the-art simulations. Unfortunately, as demonstrated in Figure 6, the total background (instrumental plus astrophysical background) reaches a value of $10^{36} \text{ erg s}^{-1} \text{ kpc}^{-2}$ at the distance of NGC 7793, hampering the detection of

the predicted hot gas corona at large radii with current data.

4.3. Implication of other physical properties

Besides the low mass, NGC 7793 is characterized by its high specific star formation rate and the very tiny bulge. We further narrow down the simulated sample by constraining the SFR and bulge fraction (derived from Du et al. 2020), in order to discuss the implication of other galaxy properties on the hot gas emission in TNG50.

The median SFR ($\overline{\text{SFR}}$) and bulge fraction ($\overline{\text{bulge}}$) of our sample is $0.36 \text{ M}_{\odot} \text{ yr}^{-1}$ and 0.18, with standard deviations of $0.2 \text{ M}_{\odot} \text{ yr}^{-1}$ and 0.08, respectively. We then divided the total sample into low ($\Delta\text{SFR} < -0.5\sigma$), moderate ($-0.5\sigma < \Delta\text{SFR} < 0.5\sigma$) and high ($\Delta\text{SFR} > 0.5\sigma$) SFR subgroups, where $\Delta\text{SFR} = \text{SFR} - \overline{\text{SFR}}$ and σ is the standard deviation of SFR. Similarly, we defined bulge subsamples as tiny ($\Delta\text{bulge} < -0.5\sigma$), normal ($-0.5\sigma < \Delta\text{bulge} < 0.5\sigma$) and large ($\Delta\text{bulge} > 0.5\sigma$) based on the bulge mass fraction ($\Delta\text{bulge} = \text{bulge mass fraction} - \overline{\text{bulge}}$), with σ representing the corresponding standard deviation. Previous studies have suggested that galaxy size determines to a great degree the galaxy evolutionary pathways (Du et al. 2021; Ma et al. 2024) and may also influence the hot gas content. However, the size of NGC 7793 is not particularly distinctive, and it is less meaningful to construct a representative sample that matches its size. Therefore we restrict our comparison to these two properties and leave a more all-sided discussions for future work.

Results for the subsamples are presented in the right column of Figure 6, in both radial and vertical perspective. It is shown that more actively star-forming subgroup tends to have more extended X-ray emission outside the disk, as the deviation from the observations at large radii increasing with higher SFR. For the inner disk emission, the high SFR subgroup aligns better with the observations, though the improvement is slight. The dependence of hot gas emission on star formation activity in spiral galaxies is predictable, as the Lx-SFR scaling relation has been established and further confirmed in a series of related works (Strickland et al. 2004; Li & Wang 2013a; Li et al. 2014). In contrast, we find that the bulge fraction does not have notable effect on the overall level of the hot gas emission. A mild improvement in alignment with the observations is seen in the tiny and normal bulge group. However, the discrepancy between observational and simulated central emission (the innermost 1 kpc) is still significant in all subgroups. In fact, even the bulgeless galaxies in TNG50 simulation host central BHs more massive than $3 \times 10^6 \text{ M}_{\odot}$, which is inconsistent with the case of NGC 7793. This man-

ifestation of the firm lower limit of black hole masses, which makes it difficult to define a sample that exactly matches the observations, is mainly due to the heavy-seed ($\gtrsim 10^5 \text{ M}_{\odot}$) MBH formation model implemented in IllustrisTNG simulations (Weinberger et al. 2018).

5. DISCUSSION

Based on the newly available data from eROSITA and the archival observations of *Chandra*, we have explored the putative hot gaseous halo of NGC 7793 and found extraplanar diffuse soft X-ray emission on both side of the galactic plane. Comparisons with TNG50 simulations suggest that stellar feedback plays a dominant role in forming and shaping the hot gas in and around low mass spiral galaxies. In theory, the hot gas can originate both externally from the IGM accretion, and/or internally from galactic feedback processes, although it is of significant difficulty to disentangle different components (e.g., the accretion-associated inflows, the feedback-associated outflows and the recycling flows) from the hybrid gas unless high resolution spectroscopy could be achieved. Here we discuss the possibilities of these two origins and examine the prediction on hot gaseous halos from TNG50 simulations and the upcoming X-ray microcalorimeter.

A generic halo of accreted IGM is predicted around present-day massive galaxies, with X-ray luminosity strongly correlated to the gravitational mass and hence scaling with the circular rotation speed of the host galaxy, as $L_X \propto V_c^{5-7}$ (Toft et al. 2002; Rasmussen et al. 2009; Crain et al. 2010). The maximal deprojected rotation velocity of NGC 7793 is $\sim 116 \text{ km s}^{-1}$ (Carignan & Puche 1990), corresponding to a 0.5–2 keV luminosity of $1 - 3 \times 10^{37} \text{ erg s}^{-1}$, which is one order of magnitude lower than the value we measured. It is not surprising given this galaxy is not so massive as the sample galaxies which Toft et al. (2002) used to derived the $L_X - V_c$ relationship. Additionally, the hot gas can escape the gravitational potential rather easily if $T > T_{\text{vir}}$, inferred to a critical temperature of $\sim 10^5 \text{ K}$ for this galaxy. Hence we conclude that the IGM accretion plays a minor role for the origin of hot gas in and around NGC 7793, and thus internal feedback must be taken into account.

It is not clear whether NGC 7793 harbors a central massive black hole which has impacted its galactic-scale hot gas. On the one hand, nearby star forming dwarf galaxies can indeed host MBHs and the evidences are not rare (Reines et al. 2011, 2013, 2020). Pannuti et al. (2011) conducted the first high-resolution X-ray study of this galaxy, which utilized a *Chandra* ACIS observation (obsID=3954) with exposure of $\sim 49 \text{ ks}$ and did not detect a central X-ray source associated with a pu-

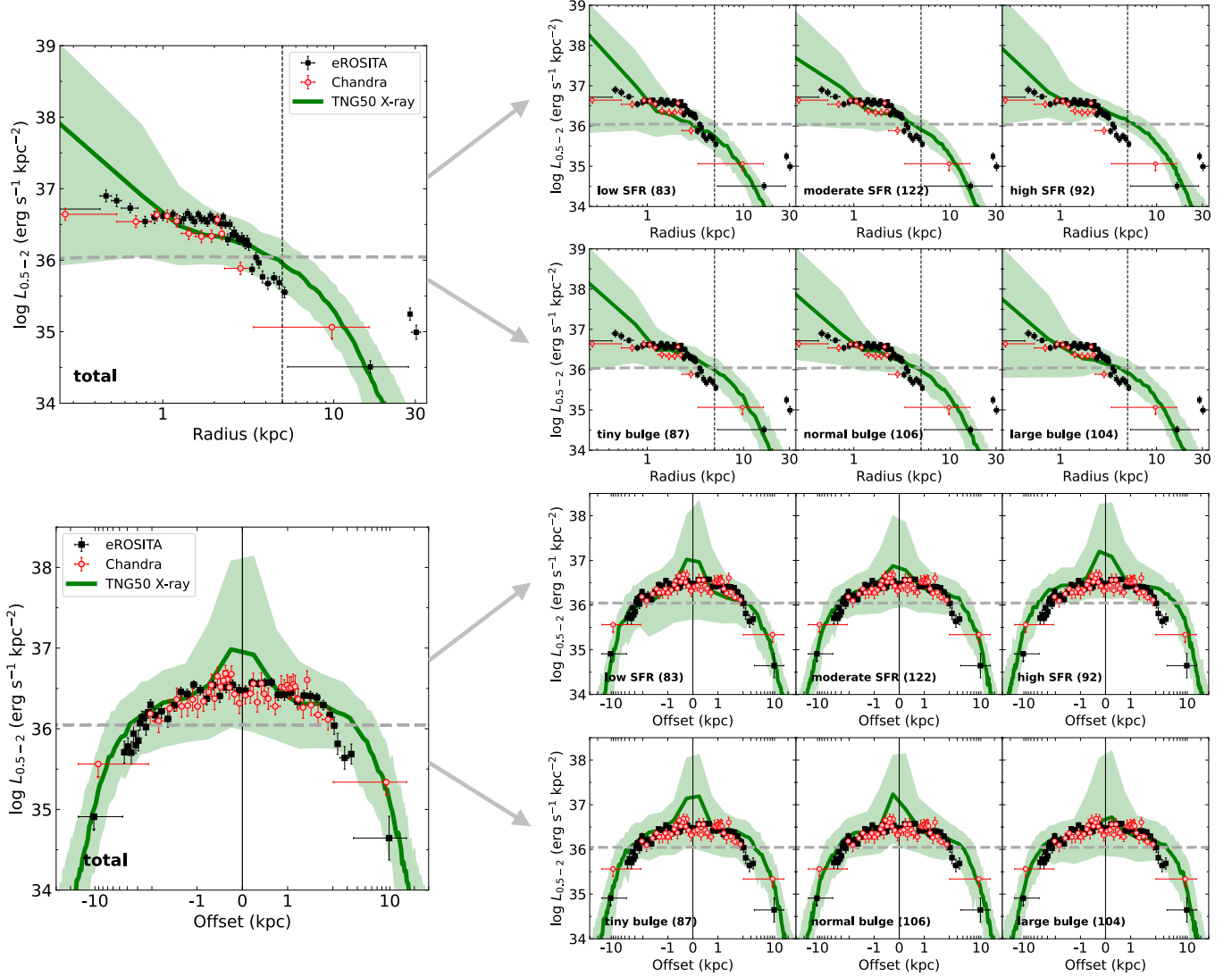


Figure 6. *Left:* Radial (Top) and vertical (bottom) X-ray luminosity profiles of the simulated galaxies resembling NGC 7793 in TNG50, comparing with the observational values (data points) after subtracting sky background. The vertical dashed line marks the R_{25} of NGC 7793, which is ~ 5 kpc in physical scale. The grey horizontal line indicates the luminosity corresponding to the total background (astrophysical and instrumental background). *Right:* Same as *Left*, but for the subgroups separating by the SFR and bulge mass fraction. The numbers in the brackets indicate the sample size of each subgroup.

tative MBH. By stacking five *Chandra* ACIS observations, we have detected an X-ray nucleus with offset of $0.8''$ from its optical center. The measured 2–10 keV luminosity is $1.25^{+0.95}_{-0.82} \times 10^{36}$ erg s^{-1} , consistent with the estimation in She et al. (2017), which was derived from the count rate by assuming an absorbed power-law model with column density inferred from the hardness ratio. This value, however, is so low that can also be powered by a normal X-ray binary. Moreover, although a nuclear star cluster (NSC) of NGC 7793 has been discovered, with a measured dynamical mass of $7.8 \times 10^6 M_{\odot}$ (Walcher et al. 2005), there is currently no robust evidence that a central MBH coexists with the NSC. Kacharov et al. (2018) compared the population

M/L ratio of this galaxy to the dynamical estimate and gave a $(M/L)_{\text{dyn}}/(M/L)_{\text{pop}} \sim 0.5$, which suggests the central MBH will be at the lower mass limit ($10^4 M_{\odot}$) if it does exist. Hence it is highly unlikely that past AGN activities play a significant role in heating and shaping the hot gas in NGC 7793.

On the other hand, stellar feedback is the most likely provider of the galactic hot gas in a star-forming galaxy, either through the stellar winds from massive stars or the core-collapse supernovae (CCSNe). Adopting a cooling function $\Lambda = 10^{-22.82}$ ergs cm^{-3} s^{-1} for temperature of $T = 10^{6.35}$ K from Sutherland & Dopita (1993), the estimated radiative cooling time for NGC 7793 is ~ 1 Gyr (the number density of electron is derived

from the APEC normalization and has a value of $\sim 0.002 \text{ cm}^{-3}$), which implies that continuous star formation can significantly contribute to the gas heating and replenishment. Indeed, there are plenty of evidence that NGC 7793 has undergone recent star-forming activities. An HST study covered almost the entire disk has identified 293 young star clusters, among which 65% is younger than 10 Myr (Grasha et al. 2018). More recently, Mondal et al. (2021) conducted an ultraviolet (UV) imaging study of this galaxy using the Ultra-Violet Imaging Telescope (UVIT) data and found around 61% of the 2046 far-UV-identified star-forming clumps have age younger than 20 Myr. Thermal energy from massive stars has been found sufficient to explain the large amount of diffuse ionized gas, which is traced by H α emission and often considered to be superposed with the X-ray-emitting hot gas (Strickland et al. 2004; Tüllmann et al. 2006a,b). From the global perspective, the moderately high SFR ($0.52 M_{\odot} \text{ yr}^{-1}$) implies a 0.5–2 keV luminosity of $3 - 13 \times 10^{38} \text{ erg s}^{-1}$ according to the Lx-SFR relation found by Li & Wang (2013a), approximately consistent with the diffuse X-ray luminosity we measured. In addition, feedback from old stellar populations can be more considerable if we assume a Type Ia SNe rate of $0.052[M_{*}/(10^{10} M_{\odot})][1/(100 \text{ yr})]$ (Mannucci et al. 2005), which amounts to a heating rate of $\sim 1.7 \times 10^{40} \text{ erg s}^{-1}$. Although this energy input rate is of two magnitude higher than the measured hot gas luminosity in this work, we note that our estimation has only considered the extraplanar parts of entire diffuse emission (i.e. the genuine hot halo) and hence omit the contribution from ISM gas, which predominates the hot gas deposit and is theoretically hotter and more metal-rich. By chiefly summing the measured hot gas luminosity in this work and Pannuti et al. (2011), the total estimate can be $\sim 5 \times 10^{38} \text{ erg s}^{-1}$, which is still much lower than the expected mechanical energy inputs from Type Ia SNe. This discrepancy can be understood as the shallow gravitational potential being insufficient to confine this hot component that a large volume of gas has been escaped out to the IGM within a rather short time. Unfortunately, given the moderate quality of the halo spectrum, it is impractical to well constrain the abundance, and the fixed sub-solar value (0.5) is likely an underestimate under the scenario of a stellar-feedback-induced metal enrichment. Higher resolution spectra are required to investigate the abundances of different elements (at least the α -to-Fe ratio), which helps to assess the respective contributions of Type II and Type Ia SNe in stellar feedback.

Furthermore, one of our incentives is to place more constraints on the modern numerical simulations by

including new measurement of the hot gaseous halo around a less massive spiral galaxy. Based on the robust detection, the hot gas emission displays a rather flat trend within the optical radius in terms of the intensity profiles. The TNG50 simulations, nevertheless, predict a brighter-than-observed core in the innermost region which approximately represents the exponential scale length of the galaxy. This can be interpreted as a sign of AGN-driven outflows in these simulated galaxies, since IllustrisTNG simulations often predict over energetic AGN activities even in the dwarf galaxies (e.g. Kristensen et al. 2021). From 1 to 3 kpc, where the emission primarily arises from the galactic plane, observations and simulations are in good agreement and further reinforce the key role of the SF-related processes in forming the hot gas. However, at larger radii where the stellar disk is truncated, the observational hot gas luminosity starts to drop faster than the simulated median values. Since our calculations related to the simulated galaxies do not consider the detection threshold, this excessive hot gas emission, even is under luminous at large distance, can always be tracked and actually deviates from real observations. We note that the total background (i.e. the astrophysical and instrumental ones) of eROSITA corresponds to a luminosity of $\sim 10^{36} \text{ erg s}^{-1}$, roughly the value at 4 kpc in the TNG50 profile, making the detection rather challenging as it joins the background and becomes less distinguishable. Nevertheless, the hot gaseous halo around NGC 7793-like galaxies can be detectable out to radius $\sim 10 \text{ kpc}$ at a level of $10^{-4} \text{ cts s}^{-1} \text{ arcmin}^{-2}$. By comparison, a study of Oppenheimer et al. (2020) has presented the predictions of hot CGM around normal galaxies using simulated eROSITA stacks in both EAGLE and Illustris-TNG simulations, with results indicating that the hot CGM can be detectable out to 30–50 kpc for intermediate-mass galaxies ($M_{*} \approx 10^{10.5} M_{\odot}$) and even 150–200 kpc for high-mass galaxies ($M_{*} \approx 10^{11} M_{\odot}$). This work, providing the latest detection of hot gas corona around a low-mass disk galaxy, can be considered as a new individual measurement which can be used to compare with the eROSITA stacking measurements, as well as a supplementary evidence for hot corona around galaxy at the low mass end.

The radial profiles of NGC 7793 exhibit a dip at $6' - 8'$, which cannot be explained by the absorption of neutral hydrogen and is more prominent in higher energy band. We have attempted to find analogous features in TNG50 simulations, i.e., the local minima in the simulated radial profiles, potentially associated with cavities in the hot gas density and X-ray luminosity maps. This phenomenon can naturally be understood as bubble-like

structures produced by past AGN outflows or multiple CCSNe embedded in the galactic disk. However, cosmological simulations help little to verify this scenario due to the relatively poor spatial and time resolution: (i) the abrupt cavities in simulations might just be an effect of the insufficient resolution in these low-mass subhalos; (ii) the time interval between the present ($z=0$) and last snapshot ($z=0.01$) is ~ 100 Myr, which makes it impossible to trace how a bubble has been blown and inflated during such a long timescale. Although the large-scale X-ray bubbles, perpendicular to the galactic disk, have been observed in the Milky Way (Predehl et al. 2020) and predicted to be common-place by numerical simulations (e.g. TNG50, Pillepich et al. 2021), we do not find any clear evidence for cavities along the vertical direction of NGC 7793 in the X-ray flux map. An exceptional bubble structure (S26, Pakull et al. 2010) inflated by a powerful microquasar has been discovered in NGC 7793, yet is much smaller (~ 300 pc) compared to the width of the dip (a few kpc). Still, two explanations are put forward for this peculiar dip: (1) It originates from a bubble-like structure, where the SNe or AGN-driven winds sweep off the hot gas, creating a cavity less dense than the interstellar medium and the surrounding CGM. (2) It is just a manifestation of the fluctuation of intragroup medium (IGrM), as NGC 7793 resides in the western end of Sculptor group.

Lastly, we examine the capability of the Hot Universe Baryon Surveyor (HUBS, Cui et al. 2020) X-ray microcalorimeter to probe the hot CGM around such low-mass galaxies. Designed to have energy resolution of 2 eV and FoV of 1 deg^2 , HUBS will be an ideal instrument to detect the emission/absorption lines associated with hot CGM and especially suited for studying galaxies at low redshifts. We make mock HUBS observations of NGC 7793-like galaxies from TNG50 simulations following Zhang et al. (2022), assuming an exposure time of 1 Ms. Each galaxy has been placed at redshift ~ 0.01 to balance the detection feasibility and the full coverage of its r_{200} . The mock X-ray images and spectra are created using the SOXS package⁴, taking into account the Galactic foreground and CXB contribution. In brief, the former is modeled as a sum of two thermal models with thermal broadening emission lines (*bapec+tbabs*bapec*), describing the Local Hot Bubble and the hot halo of our Galaxy. The latter, originating from distant AGNs and galaxies, is modeled by an absorbed power-law. We adopt a uniform radius of $10'$ for the source regions, which nearly corresponds to the r_{200}

for galaxies at $z=0.01$ and is approximate to the real observations. Pixels within the innermost $0.5'$ have been removed to exclude emission from the disk. An example of the mock spectrum is displayed in Figure 7, also shown is the zoomed-in view around the O VIII Ly α line. We use different colors and line styles to differentiate the contribution from hot CGM (red), Galactic foreground (magenta), CXB (blue) and the sum of them (grey). The redshifted lines associated with the CGM are indicated at the top of the figure. It is clear that the emission lines associated with the Galactic foreground are overwhelmingly strong over the whole wavelength range, except for some characteristic lines of the CGM (e.g. the O VIII Ly α line) that are sufficiently significant and can be captured by HUBS. We highlight that the distance of NGC 7793 is too close to probe its hot CGM, as its r_{200} (~ 100 kpc, equaling 1.5 degrees in angular) can be far exceeding the FoV of HUBS. In addition, most simulated subhalos in this work have low hot gas luminosity (less than $10^{38} \text{ erg s}^{-1}$) and hence demonstrate insignificant CGM-associated emission lines in the mock spectra, which are hard to distinguish from the foreground ones if the redshift is only 0.00076 (equals a receding velocity of 274 km/s). More specifically, we have found using mock spectra that for NGC 7793-like halos, the galaxies' O VIII Ly α lines become marginally distinguishable at redshift ~ 0.003 , and are fully separated from the foreground lines at redshift ~ 0.01 , with the resolution of 2 eV. In the meantime, the idealized targets cannot be too distant, in order to collect sufficient photons to study the properties of the low surface brightness features. Nevertheless, as is illustrated in Figure 7, HUBS is a promising probe for X-ray-emitting hot gas around nearby galaxies due to its superior energy resolution and large FoV. Both identification and characterization (e.g., temperature, metallicity, and kinematics) of the hot CGM are within grasp, provided a careful target selection.

6. SUMMARY

Based on the early released eROSITA and archival *Chandra* observations, we have studied the diffuse soft X-ray emission in and around a nearby low-mass, moderately inclined Sd galaxy, NGC 7793. Our main conclusions can be summarized as follows:

1. We have detected the extraplanar X-ray emission in energy band 0.4–2.3 keV of eROSITA, and 0.5–2 keV of *Chandra*, based on which a generically predicted hot gaseous halo is suggested. Both radial and vertical intensity profiles track the diffuse soft X-ray emission out to $5'-6'$, or 5–6 kpc from the center, more extended than the stellar disk and the H α -traced warm gas. A peculiar dip emerges at $6'-8'$ in the radial profile, yet the H I

⁴ <https://hea-www.cfa.harvard.edu/soxs/index.html>

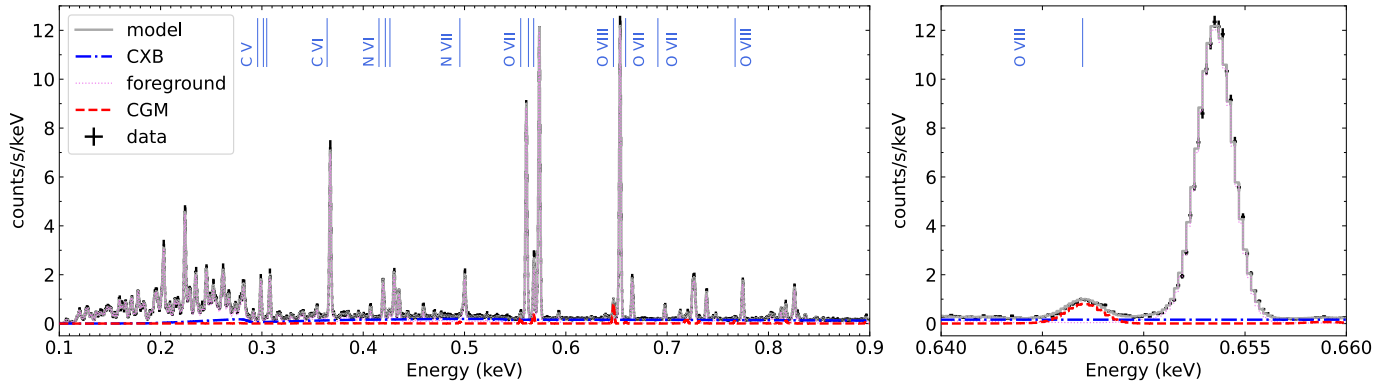


Figure 7. *Left:* Mock X-ray spectrum of an example galaxy (subhaloID=605482) in TNG50 (black), which consists of the emission from hot CGM (red), the Galactic foreground (magenta) and the CXB (blue). Emission lines associated with the hot CGM are indicated at the top. *Right:* Zoomed-in view of the spectrum around the O VIII Ly α line, which is characterized by the redshifted (assuming $z = 0.01$) line originated from the CGM and distinguishable from the foreground. The primary properties of this simulated galaxy are: (1) $M_* = 10^{9.6} M_\odot$; (2) $\text{SFR} = 1.4 M_\odot \text{ yr}^{-1}$; (3) $M_{\text{hot}} = 10^{9.7} M_\odot$.

column density profile suggests it cannot be simply explained by neutral hydrogen absorption. Two scenarios are put forward to explain this dip: (1) it arises from a bubble-like structure; (2) it is a manifestation of the fluctuated IGrM.

2. The eROSITA spectrum of the extraplanar emission can be characterized by an *apec+power-law* model, which gives a best-fit temperature of $0.18^{+0.02}_{-0.03}$ keV for the hot plasma and a photon index of $1.67^{+0.34}_{-0.38}$ for the power-law component. The estimated enclosed hot gaseous mass is $\sim 1 \times 10^7 M_\odot$, with an unabsorbed 0.5–2 keV luminosity of $1.3 \times 10^{38} \text{ erg s}^{-1}$.

3. When comparing with the hot gas emission of TNG50 simulated galaxies, observations and simulations are consistent to some degree, further strengthening the detection achieved by eROSITA and *Chandra*. However, at large radii (outside the disk), TNG50 simulations always predict excessive emission in our total sample and subsamples.

4. The estimated hot gas luminosity roughly follows the empirical L_X -SFR relation, indicating the major role of stellar feedback in forming and shaping the hot gas halo, wherein the continuous star formation is the most likely provider of the hot gas replenishment.

5. We examine the capability of HUBS to probe hot CGM around such low-mass galaxies, and find the

CGM-associated emission lines are detectable thanks to its 2 eV energy resolution and 1 deg² field of view. However, galaxies at very low redshifts such as NGC 7793 may not be ideal targets for HUBS.

ACKNOWLEDGEMENTS

This paper employs a list of Chandra datasets, obtained by the Chandra X-ray Observatory, contained in the [Chandra Data Collection \(CDC\) 356](#). L.H. would like to thank Amidou Sorgho for kindly providing the HI column density map obtained with the KAT-7 telescope, and thank Teng Liu and Xueying Zheng for helpful discussions about eROSITA data analysis. This work is supported by the National Key Research and Development Program of China (No. 2022YFF0503402), the National Natural Science Foundation of China (grant 12225302, grant 12203001), the CNSA program D050102, and the China Manned Space Program through its Space Application System. T.F is supported by the National Natural Science Foundation of China under Nos. 11890692, 12133008, 12221003, and the science research grant from the China Manned Space Project with No. CMS-CSST-2021-A04.

REFERENCES

- Anderson, M. E., & Bregman, J. N. 2011, *ApJ*, 737, 22, doi: [10.1088/0004-637X/737/1/22](https://doi.org/10.1088/0004-637X/737/1/22)
- Anderson, M. E., Bregman, J. N., & Dai, X. 2013, *ApJ*, 762, 106, doi: [10.1088/0004-637X/762/2/106](https://doi.org/10.1088/0004-637X/762/2/106)
- Anderson, M. E., Churazov, E., & Bregman, J. N. 2016, *MNRAS*, 455, 227, doi: [10.1093/mnras/stv2314](https://doi.org/10.1093/mnras/stv2314)
- Benson, A. J. 2010, *PhR*, 495, 33, doi: [10.1016/j.physrep.2010.06.001](https://doi.org/10.1016/j.physrep.2010.06.001)
- Bhattacharyya, J., Das, S., Gupta, A., Mathur, S., & Krongold, Y. 2023, *ApJ*, 952, 41, doi: [10.3847/1538-4357/acd337](https://doi.org/10.3847/1538-4357/acd337)

- Bogdán, Á., Bourdin, H., Forman, W. R., et al. 2017, *ApJ*, 850, 98, doi: [10.3847/1538-4357/aa9523](https://doi.org/10.3847/1538-4357/aa9523)
- Bogdán, Á., Forman, W. R., Kraft, R. P., & Jones, C. 2013a, *ApJ*, 772, 98, doi: [10.1088/0004-637X/772/2/98](https://doi.org/10.1088/0004-637X/772/2/98)
- Bogdán, Á., Forman, W. R., Vogelsberger, M., et al. 2013b, *ApJ*, 772, 97, doi: [10.1088/0004-637X/772/2/97](https://doi.org/10.1088/0004-637X/772/2/97)
- Bogdán, Á., Vogelsberger, M., Kraft, R. P., et al. 2015, *ApJ*, 804, 72, doi: [10.1088/0004-637X/804/1/72](https://doi.org/10.1088/0004-637X/804/1/72)
- Bomans, D. J. 2001, *Reviews in Modern Astronomy*, 14, 297, doi: [10.48550/arXiv.astro-ph/0104387](https://doi.org/10.48550/arXiv.astro-ph/0104387)
- Bothun, G. D., Eriksen, J., & Schombert, J. M. 1994, *AJ*, 108, 913, doi: [10.1086/117121](https://doi.org/10.1086/117121)
- Bothwell, M. S., Kennicutt, R. C., & Lee, J. C. 2009, *MNRAS*, 400, 154, doi: [10.1111/j.1365-2966.2009.15471.x](https://doi.org/10.1111/j.1365-2966.2009.15471.x)
- Bregman, J. N., Anderson, M. E., Miller, M. J., et al. 2018, *ApJ*, 862, 3, doi: [10.3847/1538-4357/aacafe](https://doi.org/10.3847/1538-4357/aacafe)
- Bregman, J. N., Hodges-Kluck, E., Qu, Z., et al. 2022, *ApJ*, 928, 14, doi: [10.3847/1538-4357/ac51de](https://doi.org/10.3847/1538-4357/ac51de)
- Brunner, H., Liu, T., Lamer, G., et al. 2022, *A&A*, 661, A1, doi: [10.1051/0004-6361/202141266](https://doi.org/10.1051/0004-6361/202141266)
- Calzetti, D., Lee, J. C., Sabbi, E., et al. 2015, *AJ*, 149, 51, doi: [10.1088/0004-6256/149/2/51](https://doi.org/10.1088/0004-6256/149/2/51)
- Carignan, C., & Puche, D. 1990, *AJ*, 100, 394, doi: [10.1086/115523](https://doi.org/10.1086/115523)
- Chadayammuri, U., Bogdán, Á., Oppenheimer, B. D., et al. 2022, *ApJL*, 936, L15, doi: [10.3847/2041-8213/ac8936](https://doi.org/10.3847/2041-8213/ac8936)
- Chevalier, R. A., & Clegg, A. W. 1985, *Nature*, 317, 44, doi: [10.1038/317044a0](https://doi.org/10.1038/317044a0)
- Choi, E., Brennan, R., Somerville, R. S., et al. 2020, *ApJ*, 904, 8, doi: [10.3847/1538-4357/abba7d](https://doi.org/10.3847/1538-4357/abba7d)
- Comparat, J., Truong, N., Merloni, A., et al. 2022, *A&A*, 666, A156, doi: [10.1051/0004-6361/202243101](https://doi.org/10.1051/0004-6361/202243101)
- Crain, R. A., McCarthy, I. G., Frenk, C. S., Theuns, T., & Schaye, J. 2010, *MNRAS*, 407, 1403, doi: [10.1111/j.1365-2966.2010.16985.x](https://doi.org/10.1111/j.1365-2966.2010.16985.x)
- Cui, W., Chen, L. B., Gao, B., et al. 2020, *Journal of Low Temperature Physics*, 199, 502, doi: [10.1007/s10909-019-02279-3](https://doi.org/10.1007/s10909-019-02279-3)
- Dai, X., Anderson, M. E., Bregman, J. N., & Miller, J. M. 2012, *ApJ*, 755, 107, doi: [10.1088/0004-637X/755/2/107](https://doi.org/10.1088/0004-637X/755/2/107)
- Das, S., Mathur, S., Gupta, A., & Krongold, Y. 2021, *ApJ*, 918, 83, doi: [10.3847/1538-4357/ac0e8e](https://doi.org/10.3847/1538-4357/ac0e8e)
- de Vaucouleurs, G., de Vaucouleurs, A., Corwin, Jr., H. G., et al. 1991, *Third Reference Catalogue of Bright Galaxies*
- Dicaire, I., Carignan, C., Amram, P., et al. 2008, *AJ*, 135, 2038, doi: [10.1088/0004-6256/135/6/2038](https://doi.org/10.1088/0004-6256/135/6/2038)
- Du, M., Ho, L. C., Debattista, V. P., et al. 2021, *ApJ*, 919, 135, doi: [10.3847/1538-4357/ac0e98](https://doi.org/10.3847/1538-4357/ac0e98)
- Du, M., Ho, L. C., Debattista, V. P., et al. 2020, *The Astrophysical Journal*, 895, 139, doi: [10.3847/1538-4357/ab8fa8](https://doi.org/10.3847/1538-4357/ab8fa8)
- Du, M., Ho, L. C., Zhao, D., et al. 2019, *The Astrophysical Journal*, 884, 129, doi: [10.3847/1538-4357/ab43cc](https://doi.org/10.3847/1538-4357/ab43cc)
- Foster, A. R., & Heuer, K. 2020, *Atoms*, 8, 49, doi: [10.3390/atoms8030049](https://doi.org/10.3390/atoms8030049)
- Georgakakis, A., Nandra, K., Laird, E. S., Aird, J., & Trichas, M. 2008, *MNRAS*, 388, 1205, doi: [10.1111/j.1365-2966.2008.13423.x](https://doi.org/10.1111/j.1365-2966.2008.13423.x)
- Grasha, K., Calzetti, D., Bittle, L., et al. 2018, *MNRAS*, 481, 1016, doi: [10.1093/mnras/sty2154](https://doi.org/10.1093/mnras/sty2154)
- Greco, J. P., Hill, J. C., Spergel, D. N., & Battaglia, N. 2015, *ApJ*, 808, 151, doi: [10.1088/0004-637X/808/2/151](https://doi.org/10.1088/0004-637X/808/2/151)
- Gupta, A., Kingsbury, J., Mathur, S., et al. 2021, *ApJ*, 909, 164, doi: [10.3847/1538-4357/abdbb6](https://doi.org/10.3847/1538-4357/abdbb6)
- Hou, M., Li, Z., Jones, C., Forman, W., & Su, Y. 2021, *ApJ*, 919, 141, doi: [10.3847/1538-4357/ac1344](https://doi.org/10.3847/1538-4357/ac1344)
- Hou, M., He, L., Hu, Z., et al. 2024, *ApJ*, 961, 249, doi: [10.3847/1538-4357/ad138a](https://doi.org/10.3847/1538-4357/ad138a)
- Kaaret, P., Koutroumpa, D., Kuntz, K. D., et al. 2020, *Nature Astronomy*, 4, 1072, doi: [10.1038/s41550-020-01215-w](https://doi.org/10.1038/s41550-020-01215-w)
- Kacharov, N., Neumayer, N., Seth, A. C., et al. 2018, *MNRAS*, 480, 1973, doi: [10.1093/mnras/sty1985](https://doi.org/10.1093/mnras/sty1985)
- Karachentsev, I. D., Grebel, E. K., Sharina, M. E., et al. 2003, *A&A*, 404, 93, doi: [10.1051/0004-6361:20030170](https://doi.org/10.1051/0004-6361:20030170)
- Koribalski, B. S., Wang, J., Kamphuis, P., et al. 2018, *MNRAS*, 478, 1611, doi: [10.1093/mnras/sty479](https://doi.org/10.1093/mnras/sty479)
- Kristensen, M. T., Pimblet, K. A., Gibson, B. K., Penny, S. J., & Koudmani, S. 2021, *ApJ*, 922, 127, doi: [10.3847/1538-4357/ac236d](https://doi.org/10.3847/1538-4357/ac236d)
- Lehnert, M. D., Heckman, T. M., & Weaver, K. A. 1999, *ApJ*, 523, 575, doi: [10.1086/307762](https://doi.org/10.1086/307762)
- Li, J.-T., Bregman, J. N., Wang, D., Crain, R. A., & Anderson, M. E. 2016, in *AAS/High Energy Astrophysics Division*, Vol. 15, *AAS/High Energy Astrophysics Division #15*, 402.04
- Li, J.-T., Bregman, J. N., Wang, Q. D., et al. 2017, *ApJS*, 233, 20, doi: [10.3847/1538-4365/aa96fc](https://doi.org/10.3847/1538-4365/aa96fc)
- Li, J.-T., Crain, R. A., & Wang, Q. D. 2014, *MNRAS*, 440, 859, doi: [10.1093/mnras/stu329](https://doi.org/10.1093/mnras/stu329)
- Li, J.-T., & Wang, Q. D. 2013a, *MNRAS*, 435, 3071, doi: [10.1093/mnras/stt1501](https://doi.org/10.1093/mnras/stt1501)
- . 2013b, *MNRAS*, 428, 2085, doi: [10.1093/mnras/sts183](https://doi.org/10.1093/mnras/sts183)
- Li, Z., & Wang, Q. D. 2007, *ApJL*, 668, L39, doi: [10.1086/522674](https://doi.org/10.1086/522674)
- Li, Z., Wang, Q. D., & Hameed, S. 2007, *MNRAS*, 376, 960, doi: [10.1111/j.1365-2966.2007.11513.x](https://doi.org/10.1111/j.1365-2966.2007.11513.x)

- Liu, T., Merloni, A., Wolf, J., et al. 2022, *A&A*, 664, A126, doi: [10.1051/0004-6361/202243362](https://doi.org/10.1051/0004-6361/202243362)
- Locatelli, N., Ponti, G., Zheng, X., et al. 2024, *Astronomy & Astrophysics*, 681, A78, doi: [10.1051/0004-6361/202347061](https://doi.org/10.1051/0004-6361/202347061)
- Ma, H.-C., Du, M., Ho, L. C., Sheng, M.-J., & Liao, S. 2024, *Astronomy & Astrophysics*, 689, A293, doi: [10.1051/0004-6361/202450397](https://doi.org/10.1051/0004-6361/202450397)
- Mannucci, F., Della Valle, M., Panagia, N., et al. 2005, *A&A*, 433, 807, doi: [10.1051/0004-6361:20041411](https://doi.org/10.1051/0004-6361:20041411)
- Mathews, W. G., & Baker, J. C. 1971, *ApJ*, 170, 241, doi: [10.1086/151208](https://doi.org/10.1086/151208)
- Mondal, C., Subramaniam, A., George, K., et al. 2021, *ApJ*, 909, 203, doi: [10.3847/1538-4357/abe0b4](https://doi.org/10.3847/1538-4357/abe0b4)
- Mulchaey, J. S., & Jeltema, T. E. 2010, *ApJL*, 715, L1, doi: [10.1088/2041-8205/715/1/L1](https://doi.org/10.1088/2041-8205/715/1/L1)
- Nelson, D., Springel, V., Pillepich, A., et al. 2019a, *Computational Astrophysics and Cosmology*, 6, 2, doi: [10.1186/s40668-019-0028-x](https://doi.org/10.1186/s40668-019-0028-x)
- Nelson, D., Pillepich, A., Springel, V., et al. 2019b, *MNRAS*, 490, 3234, doi: [10.1093/mnras/stz2306](https://doi.org/10.1093/mnras/stz2306)
- Oppenheimer, B. D., Bogdán, Á., Crain, R. A., et al. 2020, *ApJL*, 893, L24, doi: [10.3847/2041-8213/ab846f](https://doi.org/10.3847/2041-8213/ab846f)
- Ott, J., Walter, F., & Brinks, E. 2005, *MNRAS*, 358, 1453, doi: [10.1111/j.1365-2966.2005.08863.x](https://doi.org/10.1111/j.1365-2966.2005.08863.x)
- Pakull, M. W., Soria, R., & Motch, C. 2010, *Nature*, 466, 209, doi: [10.1038/nature09168](https://doi.org/10.1038/nature09168)
- Pannuti, T. G., Schlegel, E. M., Filipović, M. D., et al. 2011, *AJ*, 142, 20, doi: [10.1088/0004-6256/142/1/20](https://doi.org/10.1088/0004-6256/142/1/20)
- Pillepich, A., Nelson, D., Truong, N., et al. 2021, *MNRAS*, 508, 4667, doi: [10.1093/mnras/stab2779](https://doi.org/10.1093/mnras/stab2779)
- Pillepich, A., Nelson, D., Springel, V., et al. 2019, *MNRAS*, 490, 3196, doi: [10.1093/mnras/stz2338](https://doi.org/10.1093/mnras/stz2338)
- Planck Collaboration, Ade, P. A. R., Aghanim, N., et al. 2013, *A&A*, 550, A131, doi: [10.1051/0004-6361/201220040](https://doi.org/10.1051/0004-6361/201220040)
- Predehl, P., Sunyaev, R. A., Becker, W., et al. 2020, *Nature*, 588, 227, doi: [10.1038/s41586-020-2979-0](https://doi.org/10.1038/s41586-020-2979-0)
- Predehl, P., Andritschke, R., Arefiev, V., et al. 2021, *A&A*, 647, A1, doi: [10.1051/0004-6361/202039313](https://doi.org/10.1051/0004-6361/202039313)
- Rasmussen, J., Sommer-Larsen, J., Pedersen, K., et al. 2009, *ApJ*, 697, 79, doi: [10.1088/0004-637X/697/1/79](https://doi.org/10.1088/0004-637X/697/1/79)
- Read, A. M., & Pietsch, W. 1999, *A&A*, 341, 8, doi: [10.48550/arXiv.astro-ph/9810013](https://doi.org/10.48550/arXiv.astro-ph/9810013)
- Reines, A. E., Condon, J. J., Darling, J., & Greene, J. E. 2020, *ApJ*, 888, 36, doi: [10.3847/1538-4357/ab4999](https://doi.org/10.3847/1538-4357/ab4999)
- Reines, A. E., Greene, J. E., & Geha, M. 2013, *ApJ*, 775, 116, doi: [10.1088/0004-637X/775/2/116](https://doi.org/10.1088/0004-637X/775/2/116)
- Reines, A. E., Sivakoff, G. R., Johnson, K. E., & Brogan, C. L. 2011, *Nature*, 470, 66, doi: [10.1038/nature09724](https://doi.org/10.1038/nature09724)
- She, R., Ho, L. C., & Feng, H. 2017, *ApJ*, 835, 223, doi: [10.3847/1538-4357/835/2/223](https://doi.org/10.3847/1538-4357/835/2/223)
- Sorgho, A., Carignan, C., Pisano, D. J., et al. 2018, *Monthly Notices of the Royal Astronomical Society*, 482, 1248–1269, doi: [10.1093/mnras/sty2785](https://doi.org/10.1093/mnras/sty2785)
- Strickland, D. K., Heckman, T. M., Colbert, E. J. M., Hoopes, C. G., & Weaver, K. A. 2004, *ApJ*, 606, 829, doi: [10.1086/383136](https://doi.org/10.1086/383136)
- Strickland, D. K., Heckman, T. M., Weaver, K. A., Hoopes, C. G., & Dahlem, M. 2002, *ApJ*, 568, 689, doi: [10.1086/338889](https://doi.org/10.1086/338889)
- Sutherland, R. S., & Dopita, M. A. 1993, *ApJS*, 88, 253, doi: [10.1086/191823](https://doi.org/10.1086/191823)
- Toft, S., Rasmussen, J., Sommer-Larsen, J., & Pedersen, K. 2002, *MNRAS*, 335, 799, doi: [10.1046/j.1365-8711.2002.05663.x](https://doi.org/10.1046/j.1365-8711.2002.05663.x)
- Tüllmann, R., Breitschwerdt, D., Rossa, J., Pietsch, W., & Dettmar, R. J. 2006a, *A&A*, 457, 779, doi: [10.1051/0004-6361:20054743](https://doi.org/10.1051/0004-6361:20054743)
- Tüllmann, R., Pietsch, W., Rossa, J., Breitschwerdt, D., & Dettmar, R. J. 2006b, *A&A*, 448, 43, doi: [10.1051/0004-6361:20052936](https://doi.org/10.1051/0004-6361:20052936)
- Tully, R. B. 1988, *Nearby galaxies catalog*
- Veronica, A., Reiprich, T. H., Picaud, F., et al. 2024, *A&A*, 681, A108, doi: [10.1051/0004-6361/202347037](https://doi.org/10.1051/0004-6361/202347037)
- Walcher, C. J., van der Marel, R. P., McLaughlin, D., et al. 2005, *ApJ*, 618, 237, doi: [10.1086/425977](https://doi.org/10.1086/425977)
- Walker, S. A., Bagchi, J., & Fabian, A. C. 2015, *MNRAS*, 449, 3527, doi: [10.1093/mnras/stv616](https://doi.org/10.1093/mnras/stv616)
- Walter, F., Brinks, E., de Blok, W. J. G., et al. 2008, *AJ*, 136, 2563, doi: [10.1088/0004-6256/136/6/2563](https://doi.org/10.1088/0004-6256/136/6/2563)
- Weinberger, R., Springel, V., Pakmor, R., et al. 2018, *MNRAS*, 479, 4056, doi: [10.1093/mnras/sty1733](https://doi.org/10.1093/mnras/sty1733)
- White, S. D. M., & Frenk, C. S. 1991, *ApJ*, 379, 52, doi: [10.1086/170483](https://doi.org/10.1086/170483)
- White, S. D. M., & Rees, M. J. 1978, *MNRAS*, 183, 341, doi: [10.1093/mnras/183.3.341](https://doi.org/10.1093/mnras/183.3.341)
- Yoshino, T., Mitsuda, K., Yamasaki, N. Y., et al. 2009, *PASJ*, 61, 805, doi: [10.1093/pasj/61.4.805](https://doi.org/10.1093/pasj/61.4.805)
- Zhang, Y., Comparat, J., Ponti, G., et al. 2024a, *arXiv e-prints*, arXiv:2401.17308, doi: [10.48550/arXiv.2401.17308](https://doi.org/10.48550/arXiv.2401.17308)
- . 2024b, *arXiv e-prints*, arXiv:2401.17309, doi: [10.48550/arXiv.2401.17309](https://doi.org/10.48550/arXiv.2401.17309)
- Zhang, Y., Comparat, J., Ponti, G., et al. 2024, *The hot circumgalactic medium in the eROSITA All-Sky Survey III. Star-forming and quiescent galaxies.* <https://arxiv.org/abs/2411.19945>
- Zhang, Y.-N., Li, C., Xu, D., & Cui, W. 2022, *Experimental Astronomy*, 53, 1053, doi: [10.1007/s10686-022-09856-7](https://doi.org/10.1007/s10686-022-09856-7)

APPENDIX

A. THE CXB CORRECTION

We utilize the CXB $\log N$ - $\log S$ relation derived from [Georgakakis et al. \(2008\)](#) to correct a residual background in the eROSITA and *Chandra* intensity profiles, which is manifested as an uplift at large radii and can be attributed to a higher amount of unresolved CXBs at large off-axis angles. The relation follows a broken power-law form as:

$$\frac{dN}{df_X} = \begin{cases} K(f_X)^{\beta_1}, & f_X < f_b \\ K'(f_X)^{\beta_2}, & f_X \geq f_b \end{cases} \quad (\text{A1})$$

where K and K' are the normalization constants and follows the relation $K' = K(f_X)^{\beta_1 - \beta_2}$, f_b is the X-ray flux at the break point of the broken power-law, and β_1, β_2 are the power-law indices. Here f_X is in the unit of $10^{-14} \text{ erg s}^{-1} \text{ cm}^{-2}$. We adopt the parameter values in the soft band from Table 2 of [Georgakakis et al. \(2008\)](#), which are $\beta_1 = -1.58$, $\beta_2 = -2.50$, $\log(f_b/10^{-14} \text{ erg s}^{-1} \text{ cm}^{-2}) = -0.04$ and $K = 1.51 \times 10^{16} \text{ deg}^{-2}/(\text{erg s}^{-1} \text{ cm}^{-2})$.